Article

The local coordination effects on the reactivity and speciation of active sites in graphene-embedded single-atom catalysts over wide pH and potential range

Milica S. Ritopečki [1], Ana S. Dobrota [1], Natalia V. Skorodumova [2] and Igor A. Pašti [1,*]

[1] University of Belgrade – Faculty of Physical Chemistry, Studentski trg 12-16, 11158 Belgrade, Serbia; milica.ritopecki@gmail.com, ana.dobrota@ffh.bg.ac.rs, igor@ffh.bg.ac.rs

[2] Department of Materials Science and Engineering, School of Industrial Engineering and Management, KTH – Royal Institute of Technology, Brinellvägen 23, 100 44 Stockholm, Sweden, snv123@kth.se

* Correspondence: igor@ffh.bg.ac.rs; Tel.: +381 11 3336 625

Abstract: Understanding the catalytic performance of different materials is of crucial importance for further technological advancements. This especially relates to the behavior of different classes of catalysts under operating conditions. Here we analyze the effects of local coordination of metal centers (Mn, Fe, Co) in graphene-embedded Single-Atom Catalysts (SACs). We have started from well-known M@N_4-graphene catalysts and systematically replaced nitrogen atoms with oxygen or sulfur atom to obtain M@O_xN_y-graphene and M@S_xN_y-graphene SACs (x+y=4). We show that local coordination strongly affects the electronic structure and the reactivity towards hydrogen and oxygen species. However, the stability is even more affected. Using the concept of Pourbaix plots, we show that the replacement of nitrogen atoms coordinating metal center with O or S destabilizes SACs towards the dissolution, while the metal centers get easily covered by O and OH acting as additional ligands at high anodic potentials and high pH values. Thus, not only should local coordination be considered in terms of the activity of SACs, but it is also necessary to consider its effects on the speciation of SACs' active centers under different potential and pH conditions.

Keywords: single-atom catalysts; graphene; activity; reactivity; stability; Pourbaix plots;

1. Introduction

The current energy crisis has put a focus on the development of novel efficient materials for energy conversion. Electrocatalysis is expected to play a key role in this direction as it can offer many solutions in the energy race. However, electrocatalysts need to be active, stable, and affordable, facing us with the fact that no perfect solution exists so far.

One of the key strategies for lowering the catalyst price is to reduce the size of particles, ideally to nano dimensions, thus increasing the surface-to-volume ratio and the number of active sites exposed to the reaction medium. Even in this case, the cores of nanoparticles are not active. This is a waste of active components in the core. Moreover, if precious metals-based catalysts are used, it also impacts the price significantly. However, a relatively novel class of catalysts, Single-Atom Catalysts (SACs), alleviates this issue as the active site consists of only one atom. Furthermore, the active atom is embedded in a matrix that significantly impacts the activity of the active center, allowing even the alteration of reactivity trends of SACs when compared to nanosized or bulk counterparts [1-3].

SACs are usually experimentally characterized using techniques that provide resolution at the atomic level, like high-resolution transmission electron microscopy (to confirm the presence of single atoms), synchrotron-based techniques like XANES (to address local coordination) and other surface-sensitive techniques, like XPS (to observe the oxidation state of single atoms) [4]. While some of these techniques can be applied *in situ* or *in operando*, most studies consider that the structure of SACs' active sites is the

Preprints (www.preprints.org) | NOT PEER-REVIEWED | Posted: 25 November 2022 doi:10.20944/preprints202211.0475.v1

same as observed under high vacuum conditions. Nevertheless, electrocatalytic processes are typically taking place under severe conditions. For extended surface and nanosized catalysts, it is well-accepted that the surface electrochemical processes take place, like the adsorption of different spectating species, affecting the catalyst performance [5-7]. Thus, there is no reason to expect such processes not to occur at SACs used in electrocatalysis. In fact, some recent experimental and theoretical studies suggested that the adsorption of different species at active sites of SACs leads to altered catalytic activity, selectivity, and stability [8-12], or even change the nature of the active site in different media (pH) [13]. The mentioned works are particularly related to the cases of M-N_4 SACs where the metal center is embedded in a carbon lattice and coordinated by four nitrogen atoms. The class of M-N_4 SACs received a lot of attention as it turned out to be a rather promising replacement for platinum-based catalysts, while it also shows high catalytic activity for other reactions [14-17]. The most interesting metals in this sense were found to be Fe, Co, and Mn [18-20].

While it is natural to expect that some adsorption processes can take place on SACs' active centers, there are two important facts to consider. First, such processes are typically disregarded, and SACs are considered electrode potential and pH-independent systems identical to those observed under vacuum conditions. The second case is that once an adsorbate is attached to the SAC's active site, this makes a whole new active site. Namely, in the case of extended surface and nanoparticles, there are ensembles of active sites, so adsorbed species usually act as spectators – they occupy a certain number of active sites and thus reduce the activity, but a large electronic effect is usually not present [21]. However, in the case of SACs, once an adsorbate/ligand attaches to the active center, it is completely changed. Hence, as the matrix cannot be separated from the active metal atoms, the same holds for any adsorbate/ligand attached to the original active site [22].

In the present work, we complement our previous works on the stability of SACs [23], analyzing the case of M-N_4 (M = Mn, Fe, Co) centers where the metal coordination sphere is altered by systematically replacing nitrogen atoms by sulfur of oxygen. Considering the stability, we have calculated a series of standard electrode potentials for different reactions considered at the active centers and used them to construct Pourbaix diagrams [24-26] for selected cases. Furthermore, for the case of hydrogen evolution reaction (HER), we show that it is necessary to consider stability under operating conditions before providing any particular conclusions on the HER activity. Finally, we discussed possible strategies to experimentally observe SACs' active site alterations under electrochemical conditions, which are more affordable and available than *in operando* synchrotron-based techniques.

2. Materials and Methods

For the investigation of different structures and their properties, DFT calculations were used in this work utilizing Vienna Ab Initio Simulation Package, VASP [27-29]. As part of this package, Perdew-Burke-Ernzerhof form of the generalized gradient approximation functional (GGA-PBE) was combined with the projector augmented wave (PAW) method, including spin polarization [30]. Taking into account the dispersion interactions, DFT-D3 corrections were also included in the calculations [31]. Cut-off kinetic energy was set at 600 eV and the width of the Gauss smearing for all occupied electronic levels at 0.2 eV. The first irreducible Brillouin zone was obtained by forming a Γ-centered 6×6×1 k-points mesh using the general Monkhorst-Pack scheme [32]. Relaxation of the atoms in the simulation cell was enabled until the value of the Hellmann-Feynman forces that act on them would not drop below 0.01 eV $Å^{-1}$. All of the shown models of the structures in this work were made with the Visualisation for Electronic Structural Analysis program (VESTA) [33].

The starting structure of pyridine-N_4 graphene was modelled by first forming the di-vacancy in the 4×4 supercell of pristine graphene with 32 C atoms – a defect that is

Preprints (www.preprints.org) | NOT PEER-REVIEWED | Posted: 25 November 2022 doi:10.20944/preprints202211.0475.v1

made by removing two neighboring carbon atoms. Then, the four closest carbon atoms were replaced by nitrogen atoms. The model that is created this way has the following formula: N_4C_{26}. In the next step, one, two, or three of these nitrogen atoms were replaced with either oxygen or sulfur atoms. Finally, systems with metals were obtained by embedding the transition metal atoms that showed good results in the previous works into investigated structures – manganese, iron, and cobalt [23].

The embedding energy of the metals, $E_{emb}(M)$, was calculated as:

$$E_{emb}(M) = E(M@X_xN_yG) - E(X_xN_yG) - E(M). \quad (1)$$

Here, $E(M@X_xN_yG)$ represents the energy of the system that contains metal, $E(X_xN_yG)$ energy of di-vacant pyridine-like graphene, and $E(M)$ energy of the isolated metal atom, while x and y are natural numbers, such that x+y=4. It should be considered that X stands for either O, or S atom, depending on the corresponding system.

Depending on the experimental conditions, different surface functionalization can occur during synthesis – hydrogen, oxygen, or hydroxyl group adsorption. These adsorption reactions can be represented electrochemically (all written as half-reactions in the direction of reduction):

$$M^{z+} + ze^- + X_xN_yG \rightarrow M@X_xN_yG, \quad (2)$$

$$M@X_xN_yG + H^+ + e^- \rightarrow H–M@X_xN_yG \quad (3)$$

$$OH–M@X_xN_yG + H^+ + e^- \rightarrow M@X_xN_yG + H_2O \quad (4)$$

$$O–M@X_xN_yG + 2H^+ + 2e^- \rightarrow M@X_xN_yG + H_2O. \quad (5)$$

Adsorption energies $E_{ads}(A)$, which describe bond formation between adsorbate and inquired systems, are calculated as:

$$E_{ads}(A) = E_{subs+A} - (E_{subs} + E_A) \quad (6)$$

Here, the energy of the substrate with adsorbed atom or group is E_{subs+A}, the energy of the substrate is E_{subs}, and the energy of the isolated adsorbate A (A = H, O or OH) is E_A.

In order to examine an additional thermodynamic aspect of the obtained systems, vibrational analysis was also performed. The approach of interrogation of the second-order finite differences was used, and the displacements in all three directions were set to be 0.015 Å. However, to save some computational time, the constrained dynamics was utilized where the displacements were limited to metal atoms, nitrogen/oxygen/sulfur atoms, and carbon atoms that formed a bond with them, i.e., only the first and the second coordination spheres of the metal center was considered for vibrational analysis.

The obtained values of the vibrational frequencies are used to calculate the thermodynamics functions, such as zero-point energies (ZPE) and vibrational contributions to the entropy, TS_{vib}. Then, the chemical potential, μ_i, was obtained for each phase in the electrochemical equations (2)-(5):

$$\mu_i = E_{tot} + ZPE - TS_{vib} \quad (7)$$

Here, E_{tot} stands for the energy of the given phase obtained using DFT.

It should be noted that the chemical potential of pure water was calculated in the gas phase at a temperature of 298 K and pressure of 1 atm, and the obtained value was additionally corrected using the Gibbs free energy change corresponding to evaporation under the same conditions as listed.

Based on these results, Gibbs free energy change for reactions (2)-(5), ΔG, was calculated:

$$\Delta G = \sum_{i,\text{products}} \mu_i - \sum_{i,\text{reactants}} \mu_i \quad (8)$$

Preprints (www.preprints.org) | NOT PEER-REVIEWED | Posted: 25 November 2022 doi:10.20944/preprints202211.0475.v1

The downside of using the constrained dynamics can be seen when calculating ΔG – the obtained value is smaller by 0.03-0.05 eV than the value obtained without constraints [23].

In this paper, a hypothetical galvanic cell was used, where the reactions of interest take place on the cathode, while the hydrogen electrode represents the anode. By keeping this in mind and assuming the equilibrium of the hydrogen electrode (reference potential of the hydrogen electrode is set in that manner that the electrochemical potential of the ($H^+ + e^-$) system is the same as the potential of ½ H_2 in the following conditions: T = 298 K, p = 1 atm, and pH = 0):

$$H^+ + e^- \rightarrow ½\ H_{2\,(g)}, \quad (9)$$

the standard electrode potentials were calculated (*vs.* Standard Hydrogen electrode, SHE) for electrochemical reactions (2)-(5). This was done by utilizing the Computational Hydrogen electrode approach [34].

Based on the value of the Gibbs free energy change, the electromotive force for each reaction (2)-(5) was also calculated by simply dividing ΔG by the number of electrons exchanged in the system during the corresponding reaction. Since, as mentioned, the hydrogen electrode represents the anode, the electromotive force is equal to the standard electrode potential of the given reaction. A somewhat different system is considered for the metal embedding reactions – a hypothetical galvanic cell where one electrode is made ~~out~~ of the transition metal in question, and the other is the given M@X_xN_yG electrode [23].

Finally, optical spectra were calculated from the frequency-dependent microscopic polarizability matrix in the projector-augmented wave (PAW) methodology [35].

3. Results and Discussion

3.1. Embedding Co, Fe and Mn into X_xN_y-graphene

Embedding the chosen metal atoms into the mixed X_xN_y-centres results in the formation of M@X_xN_yG surfaces. The optimized structures of M@X_xN_yG show similar general characteristics for the same X_xN_y-centre for all three metals. As an example, the structures of Fe@X_xN_yG are shown in **Fig. 1**, (**b**). While the O-containing M@X_xN_yG systems remain planar, the S-containing models show a significant protrusion of S and its first neighbors from the graphene plane. Of course, depending on the metal, the M–X bond lengths change. The average bond lengths between M and its first neighbors are given in **Table 1**. The corresponding bond lengths change in the order Mn > Fe > Co, which can be attributed to the differences in the metals' radii.

Table 1. Average bond lengths (d) between metal M and its first neighbors in M@X_xN_yG systems.

M	Systems containing O		Systems containing S	
	d(M–N) / Å	d(M–O) / Å	d(M–N) / Å	d(M–S) / Å
Co	1.85	1.92	1.91	2.08
Fe	1.87	1.92	1.92	2.12
Mn	1.89	1.94	1.94	2.20

The embedding energies of M@X_xN_yG are shown graphically in **Fig. 1**, (**a**). In order to evaluate the stability of the M single atoms in X_xN_yG, we compare these energies with the cohesive energies of the corresponding metals, E_{coh}(M). Co is found to be stable in all the investigated X_xN_y-centres. For ON_3 and SN_3 mixed centers, E_{emb}(M) surpasses E_{coh}(M) for all three metals, *i.e.*, the metals are more stable in X_xN_yG than they would be in the bulk metal lattice. However, that is not the case for Mn and Fe in other investigated mixed centers, where some metal aggregation could be possible. We notice that for one X_xN_yG center, the embedding energies follow the general trend $|E_{emb}(Co)| > |E_{emb}(Fe)| >$

Preprints (www.preprints.org) | NOT PEER-REVIEWED | Posted: 25 November 2022 doi:10.20944/preprints202211.0475.v1

$|E_{emb}(Mn)|$. Calculated $|E_{emb}(M)|$ are generally lower than those of N_4-graphene [23]. Higher O-content in O_xN_y is found to have a weakening effect on $E_{emb}(M@O_xN_yG)$.

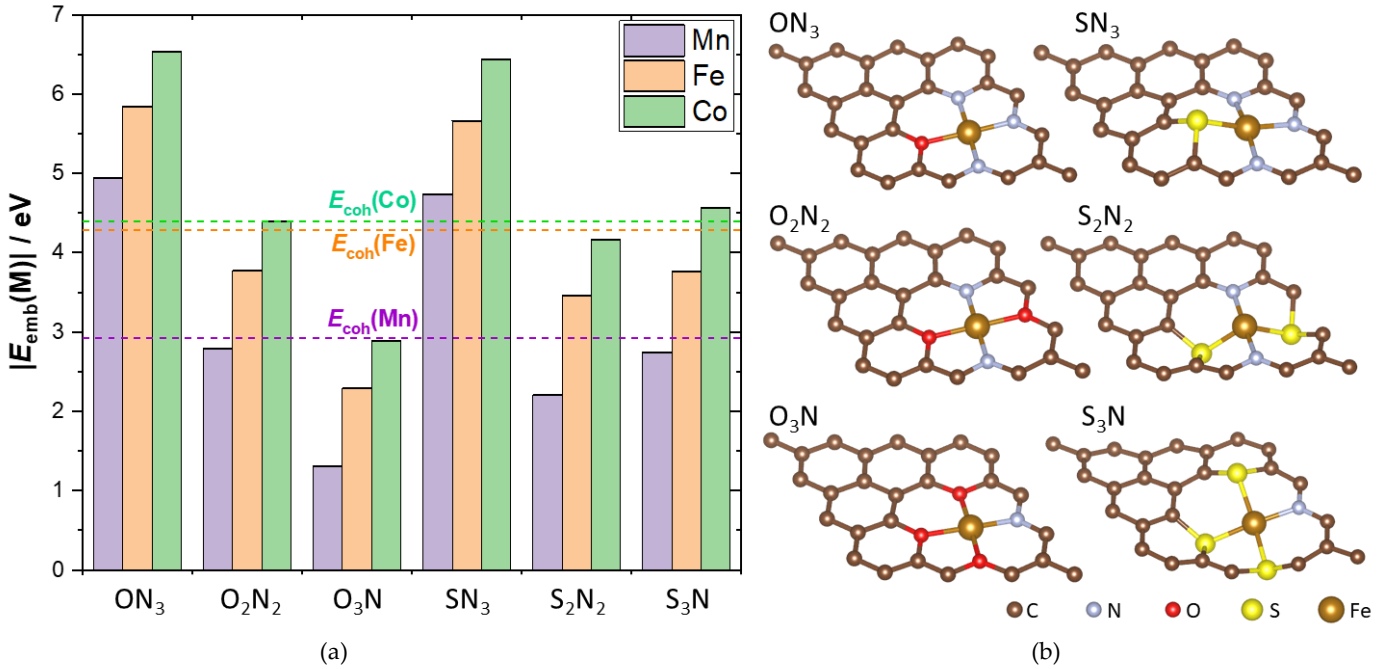

(a) (b)

Figure 1. (a) Embedding energies of Mn, Fe and Co into X_xN_y-graphene. The composition of the X_xN_y-centres is given on the *x*-axis. Cohesive energies of the three metals (taken from Ref. [36]) are shown as dashed horizontal lines, for comparison; (b) optimized structures of $Fe@X_xN_yG$. The composition of the X_xN_y moiety is given above each inset.

3.2. H, O and OH adsorption on M@X_xN_yG

Next, we investigated the adsorption of H, O and OH onto $M@X_xN_yG$ systems shown above at the M-top adsorption site (directly above the metal atom). First, let us focus on the adsorption of atomic hydrogen. The strongest H binding is found in the case of $H@Mn@S_2N_2G$, with $E_{ads}(H)$ amounting to –2.65 eV. For nearly all the investigated systems, we find that for the same X_xN_y center $E_{ads}(H@M@X_xN_yG)$ follows the trend $|E_{ads}(H@Fe@X_xN_yG)| > |E_{ads}(H@Mn@X_xN_yG)| > |E_{ads}(H@Co@X_xN_yG)|$, *i.e.*, H adsorption is the strongest when Fe is embedded in the given center, and the weakest for Co (**Fig. 2**). The only exception from this trend is the S_2N_2 centre, for which H binding is the strongest when M is Mn, and weakest for Fe. Comparing the studied systems with their N_4-analogues, we find that Co embedded in the mixed centers binds hydrogen weaker than in the N_4-case, while for Mn and Fe, it can be both stronger and weaker, depending on the nature of the chosen center.

Preprints (www.preprints.org) | NOT PEER-REVIEWED | Posted: 25 November 2022 doi:10.20944/preprints202211.0475.v1

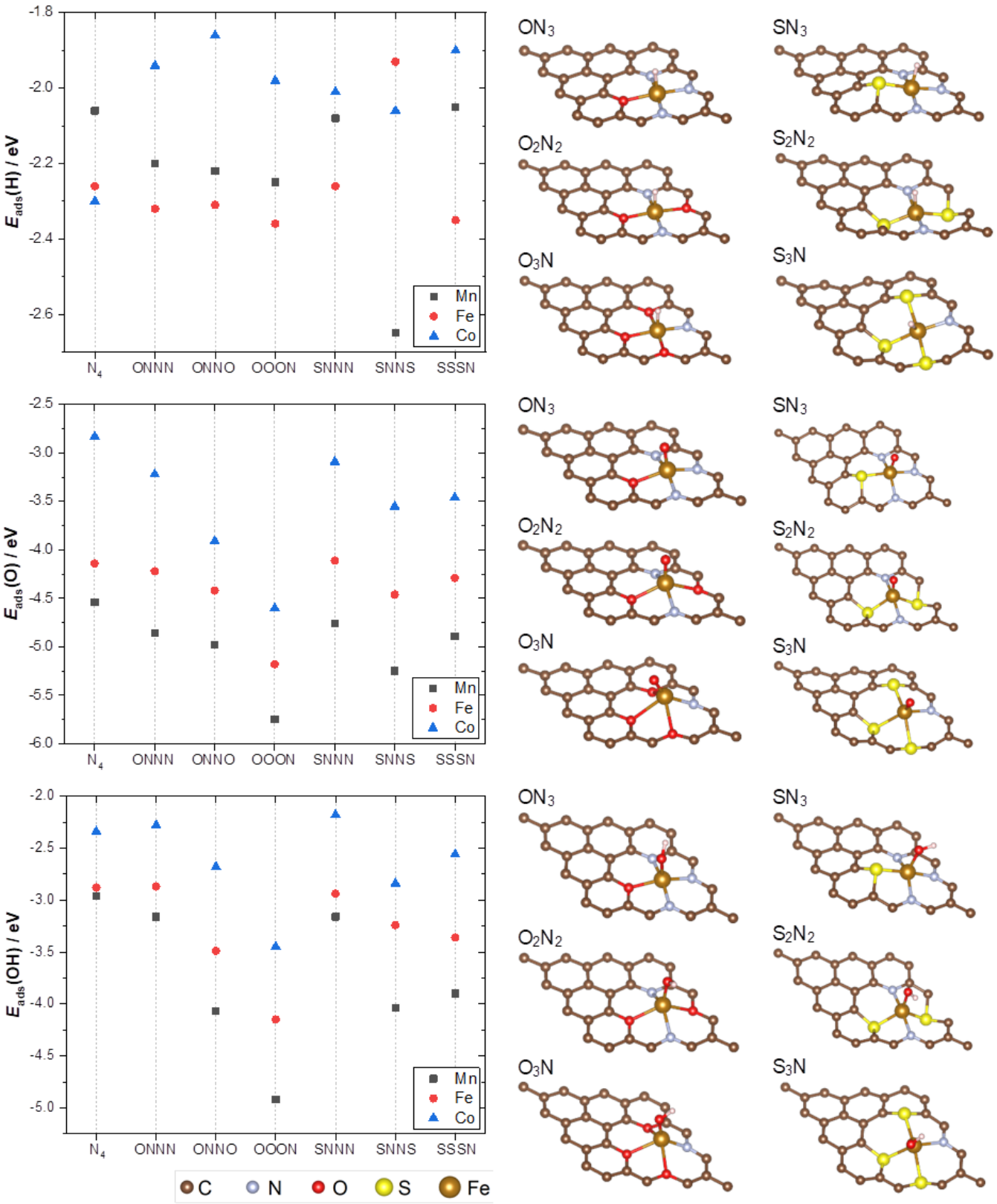

Figure 2. Left: adsorption energies of H (top), O (middle) and OH (bottom) on M@X_xN_y-graphene models (M = Mn, Fe or Co, as indicated in the legend). The composition of the mixed X_xN_y-center is given on the *x*-axis. The corresponding adsorption energies on M@N_4G are given for comparison (values from Ref. [23]). Right: optimized structures of A@Fe@X_xN_y-graphene (A = H, O or OH).

Regarding the O adsorption, all the investigated systems show stronger O binding than their N_4 analogs, except for O@Fe@SN_3G, for which O binding is weaker by approx. 0.03 eV. The strongest O binding is found for O@Mn@O_3NG, with E_{ads}(O) amounting to –

Preprints (www.preprints.org) | NOT PEER-REVIEWED | Posted: 25 November 2022 doi:10.20944/preprints202211.0475.v1

5.75 eV. As a general trend for O adsorption on O-containing mixed centers in graphene, we find that higher O-content in the mixed center yields stronger O binding onto M for all three investigated metals. On the other hand, for S-containing mixed centers, we find that the strongest O-binding corresponds to M@S_2N_2G systems.

Finally, for the case of OH adsorption, the strongest binding is found for OH@Mn@O_3NG (same system as for O_{ads}), with E_{ads}(OH) equal to –4.92 eV. The OH adsorption is found to follow nearly the same trends as O adsorption, with the only difference being that for Fe embedded into S-containing mixed centers, OH binding grows stronger with increasing S content. For all Mn@X_xN_yG, OH binding is stronger than on Mn@N_4G. This is also true for most Fe- and Co-containing centers, compared to Fe@N_4G and Co@N_4G. While H adsorption induces minimal deformation of M@X_xN_yG, the adsorption of O and OH causes larger protrusions of M and its surrounding atoms (**Fig. 2**, right).

3.3. Thermodynamics & Electrochemistry

We investigated redox pairs M^{z+}/M@X_xN_yG, M@X_xN_yG/H–M@X_xN_yG, OH–M@X_xN_yG/M@X_xN_yG, and O–M@X_xN_yG/M@X_xN_yG and calculated their standard potentials (E^0(O/R)) and equilibrium potentials (E(O/R)), at the standard conditions and at 298 K. This was done using the ground state energies, *ZPE* and entropic contributions for M@X_xN_yG, H–M@X_xN_yG, HO–M@X_xN_yG and O–M@X_xN_yG systems. The calculated standard potentials (E^0(O/R)) are summarized in **Table 2**.

Table 2. Calculated standard electrode potentials for reactions in Eq. (2) - (5) at T = 298 K, pH = 0.

System	E^0 (M^{z+}/MX_xN_yG) / V	E^0 (MX_xN_yG/H–MX_xN_yG) / V	E^0(OH–MX_xN_yG/ MX_xN_yG) / V	E^0(O–MX_xN_yG/ MX_xN_yG) / V
Co@ON_3G	0.356	–0.548	1.133	1.166
Co@O_2N_2G	–0.716	–0.596	0.718	0.913
Co@O_3NG	–1.455	–0.452	–0.137	1.070
Co@SN_3G	0.304	–0.450	1.204	1.211
Co@S_2N_2G	–0.845	–0.409	0.604	1.380
Co@S_3NG	–0.617	–0.579	0.802	1.332
Fe@ON_3G	0.288	–0.157	0.482	0.855
Fe@O_2N_2G	–0.735	–0.174	–0.118	1.266
Fe@O_3NG	–1.487	–0.149	–0.859	1.165
Fe@S_3G	0.206	–0.229	0.431	1.031
Fe@S_2N_2G	–0.893	–0.564	0.200	0.916
Fe@S_3NG	–0.731	–0.150	–0.030	1.286
Mn@ON_3G	–0.228	–0.301	0.161	0.533
Mn@O_2N_2G	–1.296	–0.256	–1.077	1.668
Mn@O_3NG	–2.037	–0.215	–1.635	1.369
Mn@SN_3G	–0.314	–0.415	0.191	0.641
Mn@S_2N_2G	–1.602	0.268	–0.700	0.991
Mn@S_3NG	–1.298	–0.482	–0.562	1.217

Metal dissolution, Eq. (2) is not pH-dependent, but the adsorption of H, O and OH are, with the slope of E *vs*. pH line of 59 mV *per* pH unit:

$$E(M^{z+}/M@X_xN_yG) = E^0(M^{z+}/M@X_xN_yG) + (0{,}059\ V / z) \cdot \log a(M^{z+}), \quad (10)$$

$$E(M@X_xN_yG/H–M@X_xN_yG) = E^0(M@X_xN_yG/H–M@X_xN_yG) – 0.059\ V \times pH \quad (11)$$

$$E(OH–M@X_xN_yG/M@X_xN_yG) = E^0(OH–M@X_xN_yG/M@X_xN_yG) – 0.059\ V \times pH \quad (12)$$

Preprints (www.preprints.org) | NOT PEER-REVIEWED | Posted: 25 November 2022 doi:10.20944/preprints202211.0475.v1

$$E(\mathrm{O–M@X_xN_yG/M@X_xN_yG}) = E^0(\mathrm{O–M@X_xN_yG/M@X_xN_yG}) - 0.059\ \mathrm{V} \times \mathrm{pH}. \quad (13)$$

We used $a(M^{z+})=10^{-8}$ mol dm^{-3} and calculated E(O/R) for pH values from 0 to 14, which allowed us to identify the stable phases for each E/pH combination, based on the rule that the most stable oxidized phase is the one with the lowest equilibrium potential, while the most stable reduced phase is the one with the highest equilibrium potential. When we apply this rule to pH=0, looking at the standard electrode potentials (**Table 2**), we see that ON_3 and SN_3 are the only X_xN_y-centres in which Fe and Co are stable, and would not dissolve ($E^0(M^{z+}/MX_xN_yG) > E^0(H^+/H_2)$). In addition, we notice a trend – a larger atomic number of M (Z(Mn) < Z(Fe) < Z(Co)) yields a more stable system (M embedded instead of dissolved). A similar was previously reported for N_4-graphene [23].

Since $E(M^{z+}/M@X_xN_yG)$ does not depend on pH, while other equilibrium potentials do, an increase in pH will enable $E(M^{z+}/M@X_xN_yG)$ to be greater than $E(M@X_xN_yG$ /H–$M@X_xN_yG)$, even though that was not the case for pH=0. When that is true, systems with adsorbed H are stable. A similar could happen with adsorbed O or OH. The lowest pH values for which H, O or OH will cover M are given in **Table A1**. However, it should be noted that the nature of the most stable phase depends not only on pH but also on the electrode potential. Therefore, this table only provides us with the pH range for which it is possible to obtain the adsorbed species at any E. In the case of Fe, hydrogen will not cover $Fe@O_3NG$, and OH will adsorb only on the $Fe@ON_3G$ and $Fe@SN_3G$ systems at pH values of 7.29 and 7.81, respectively. Oxygen adsorption can only be achieved with one system with Fe – $Fe@ON_3G$ at a very high pH (13.61). In the case of manganese, unlike cobalt and iron, hydrogen adsorption occurs only on two systems - $Mn@ON_3G$ and $Mn@SN_3G$. However, the hydroxyl group is adsorbed on four out of six systems – adsorption does not occur with $Mn@S_2N_2G$ and $Mn@S_3NG$. Oxygen cannot be adsorbed on any system.

The data acquired in the previous work [23] and the ones presented here can be used to screen the catalytic performance of studied SACs toward HER. To do this, we follow the work of Nørskov et al. [37] and use calculated ΔG for H_{ads} formation to construct the HER reaction profiles. The data for Pt(111), serving as a reference, are taken from Ref. [37]. **Fig. 3** assembles several SACs where low HER overvoltages should be observed based on the calculated $\Delta G(H_{ads})$.

The presented systems with Fe centers show that the formation of H_{ads} requires energy input. Thus, H_{ads} will be formed at potentials below 0 vs. RHE. However, compared to the well-known $Fe@N_4G$ system, activity improvements are expected for $Fe@ON_3G$, $Fe@O_3NG$, and $Fe@S_3NG$, while $Fe@SN_3G$ should display the HER activity very similar to that of $Fe@N_4G$. Nevertheless, based on the potential presented in **Table 2**, $Fe@O_3NG$ and $Fe@S_3NG$ systems should not be stable at 0 V vs. RHE. Thus, the metal center would dissolve in highly acidic media, which corresponds to the considered HER conditions. Moreover, going back to **Fig. 1**, one can see that for $Fe@O_3NG$ and $Fe@S_3NG$ systems, E_{emb}(Fe) is also below the Fe cohesive energy. This not only means that the metal centers could dissolve under HER conditions but also that some Fe aggregation could be expected during the synthesis of such SACs. This observation reinforces the conclusion that the active centers' stability must be considered before assessing the activity.

Preprints (www.preprints.org) | NOT PEER-REVIEWED | Posted: 25 November 2022 doi:10.20944/preprints202211.0475.v1

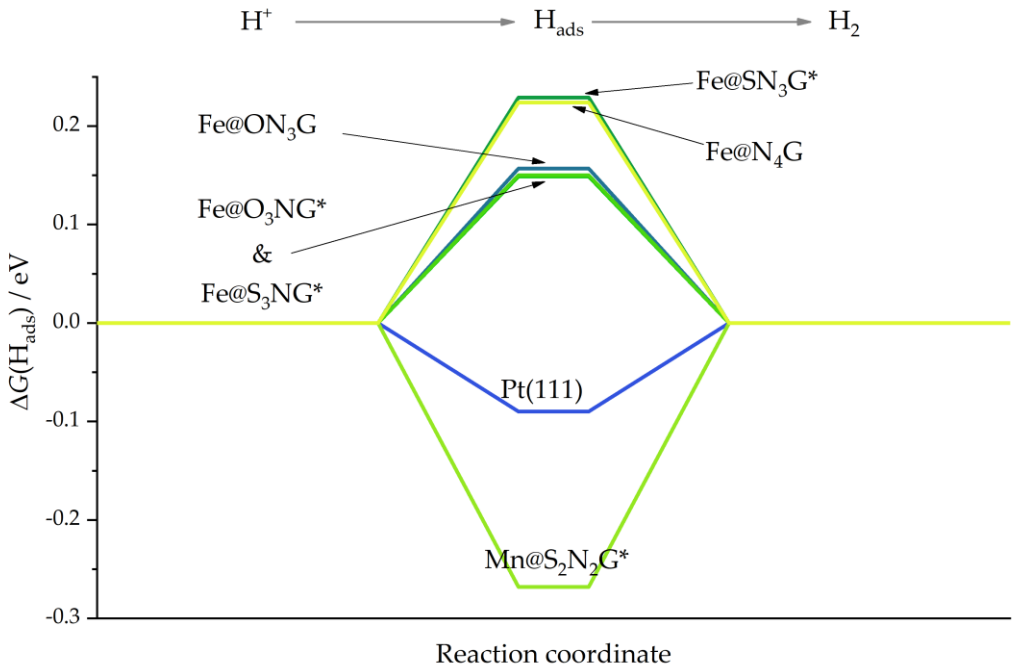

Figure 3. HER reaction profiles for selected systems. The ones marked with (*) are not stable at 0 V vs. Reversible Hydrogen Electrode.

In addition to the stability, one should also consider the speciation of SACs' active centers under different reaction conditions. Thus, finally, we constructed surface Pourbaix diagrams, allowing us to easily see which phase is the most stable for given *E* and pH. We choose two systems, Fe@ON$_3$G and Fe@SN$_3$G (**Fig. 4**), which should be relatively stable in a wide range of pH and electrode potentials, as one might expect based on the data presented in **Table 2**. In fact, Co and Fe at ON$_3$ and SN$_3$ centers are found to be the only stable metal atoms at pH=0 among all the studied cases. Fe center was previously found stable at the N$_4$-centre in graphene for all pH [23]. We find that in the case of the mixed X$_x$N$_y$ centers, dissolution is possible, but we also find regions where Fe@X$_x$N$_y$G is stable and where adsorbed H or OH are stable.

Considering the results presented in **Fig. 4**, one can see that both systems could easily dissolve at potentials close to 0 V vs. RHE (please, note that the Nernst potential for dissolution was calculated from the standard potentials and assuming Fe concentration (activity) of 10^{-8} mol dm^{-3} which shifts the equilibrium potential to lower values). At pH above 8, both systems tend to adsorb OH rather than getting dissolved. However, this also means that under oxygen reduction reaction conditions, both centers should bind OH$_{ads}$, and the reaction is likely to proceed at the active site, which is not bare as in a vacuum. Therefore, natural questions arise regarding the stability and activity of such modified active centers. Such questions have been tackled recently by Nematollahi *et al.* [12], showing that in the case of Fe-N$_4$ centers, a fifth ligand such as −NH$_2$, −OH, and −SO$_4$ can improve stability and direct oxygen reduction reaction towards selective 4e reduction pathway. This means that it is necessary to consider other possible adsorbates that can tune the active centers' electronic structure, stability and reactivity. However, it is more than obvious that the electronic structure of active centers is particularly affected by the presence of different adsorbates (**Fig. 5**). At first glance, for Fe@ON$_3$G and Fe@SN$_3$G systems, it seems that the electronic structures of the bare metal center are mutually similar, and it is mainly determined by nitrogen ligands. The same holds for the centers with H$_{ads}$. However, the situation is different for the Fe centers with OH$_{ads}$ and O$_{ads}$, which is also reflected in somewhat different oxidation potentials, particularly for O$_{ads}$-Fe cases.

Preprints (www.preprints.org) | NOT PEER-REVIEWED | Posted: 25 November 2022 doi:10.20944/preprints202211.0475.v1

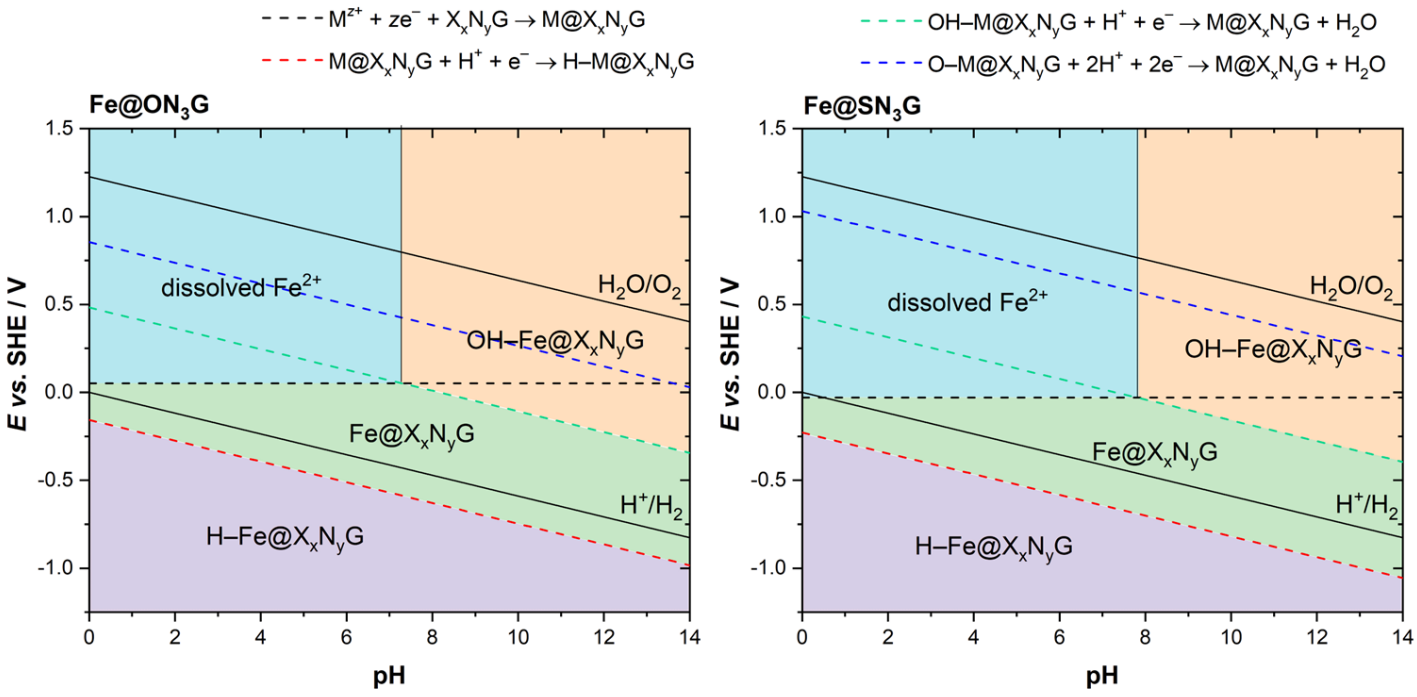

Figure 4. Surface Pourbaix plots for (a) Fe@ON$_3$-graphene and (b) Fe@SN$_3$-graphene model systems. Solid black lines (H^+/H_2 and H_2O/O_2) indicate the theoretical water stability region.

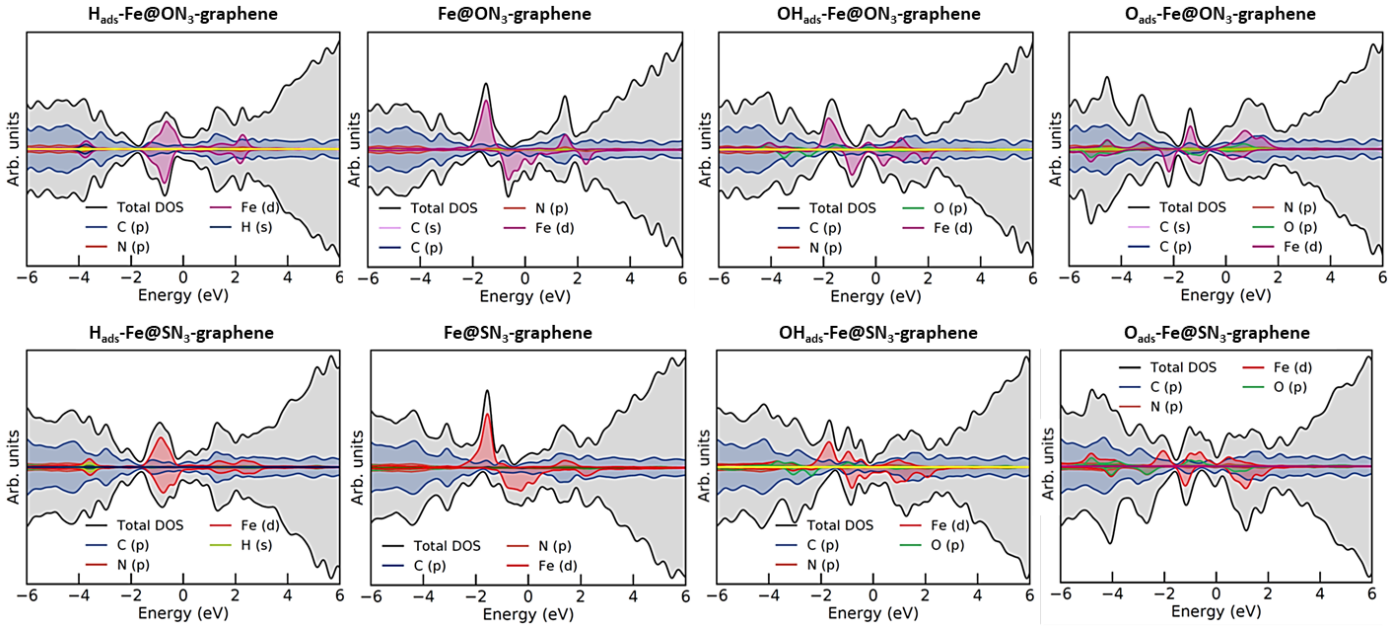

Figure 5. Densities of States (DOS) for the Fe@ON$_3$ system (top row) with H$_{ads}$, bare metal center, OH$_{ads}$, and O$_{ads}$, in that order from left to right, and the analogous DOS plots for the Fe@SN$_3$ system (bottom row). The DOS plots were generated using sumo-tools for VASP [38].

3.4. Observing active center change

As mentioned, there are direct experimental pieces of evidence that SACs' active centers might differ from their "pristine" forms under operating conditions. For example, using *in operando* XANES and FT-EXAFS [11], it was shown that under oxygen reduction reaction conditions, OH$_{ads}$ is formed at the Fe-N$_4$ center. As we discussed previously [23], synchrotron-based techniques are not widely available, particularly *in situ* and *in operando*. However, to show that the active center has changed under potential cycling or due to the pH of the environment, it might be so that less sophisticated techniques are

Preprints (www.preprints.org) | NOT PEER-REVIEWED | Posted: 25 November 2022 doi:10.20944/preprints202211.0475.v1

sufficient, at least to demonstrate qualitative change. We have previously suggested in situ FTIR as a possible option, where the characteristic bands could be used to confirm the formation of some adsorbate species at the metal centers or carbon matrix [23]. On the other hand, **Fig. 5** clearly demonstrates that the electronic structure of SACs near the Fermi level changes upon adsorption of different species. Thus, one might expect that the optical properties of SACs will also change in the case of the potential modulation or pH change, leading to the dissolution of metals or adsorption at metallic sites. **Fig. 6** shows calculated UVC-Vis-NIR spectra (from 200 nm – 1000 nm) of bare Fe@ON_3G, systems with H_{ads}, O_{ads}, and OH_{ads}, but also an empty ON_3G moiety, corresponding to the situation when the Fe center is expected to dissolve (pH < 7 and potentials above 0 V vs. RHE, **Fig. 4**). We notice that the use of UV-Vis spectroscopy for the study of porphyrins is rather widespread, and it is sensitive to the coordination of metal center [39-41].

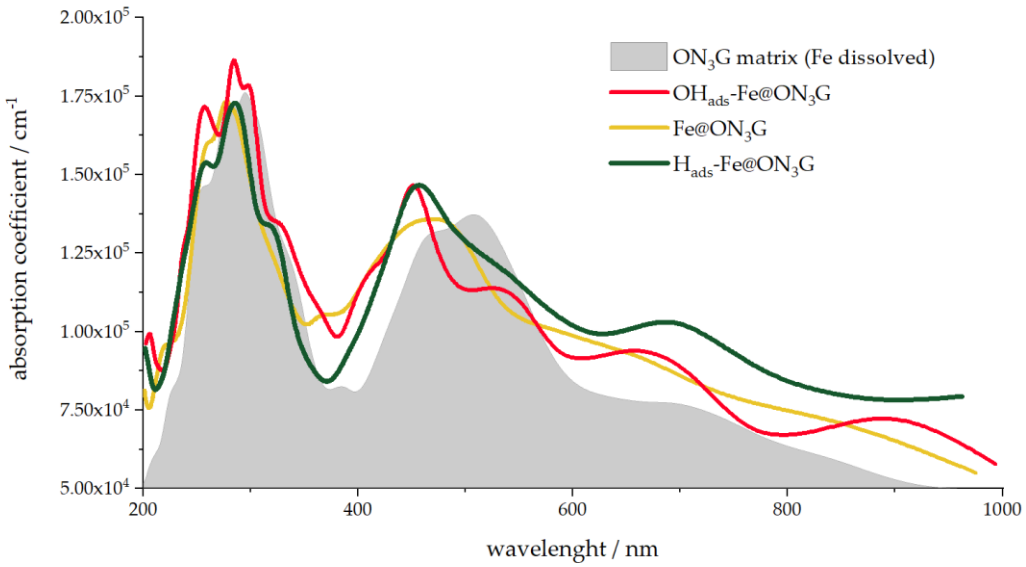

Figure 6. Optical spectra of Fe@ON_3G SACs (bare, H_{ads}-, and OH_{ads}-covered centers) and the spectrum of the corresponding ON_3G matrix, analogous to the case when the metal center is dissolved.

Obviously, the changes in the presented optical spectra (**Fig. 6**) are prominent enough at least to confirm the changes in the active site structure. Although optical spectroscopy is not as informative as FTIR and more advanced techniques and cannot easily identify the actual structure of the active site, we believe it has certain advantages. Namely, the technique is inexpensive and rather fast, while it can also be performed *in situ*, without problems caused by the adsorption of incident light by water. Thus, with many existing spectroelectrochemical systems commercially available, it would be relatively easy to use UV-Vis spectroscopy in situ and *in operando*, at least to indicate that changes are taking place at the SACs' active centers.

5. Conclusions

In the present work, we have addressed the role of metal center coordination in SACs comprised of Mn, Fe, and Co, embedded in O_xN_yG or S_xN_yG moiety in the graphene basal plane (x+y=4). Compared to the well-known M@N_4 SACs studied before, the SACs with mixed coordination of metal centers show altered embedding energies, reactivity and stability. First of all, for systems with a low number of N atoms coordinating metal centers, the embedding energies are higher than cohesive energy, suggesting that metal precipitation might occur. However, even if metal precipitation can be avoided, the metal centers are prone to dissolution and show altered reactivity compared to M@N_4 counterparts. We have shown that replacing a certain number of N atoms in the Fe coordination shell with O or S can tune hydrogen binding energy and

Preprints (www.preprints.org) | NOT PEER-REVIEWED | Posted: 25 November 2022 doi:10.20944/preprints202211.0475.v1

improve HER activity compared to the original Fe@N_4 SAC. However, it is much more important to emphasize that only a few of these systems with expectedly improved HER activity (relying on descriptor-based estimations) are actually stable at low pH (~ 0). Other systems are expected to dissolve under HER operating conditions. Thus, one of the main messages is that the estimation of the catalyst activity should be considered only if the stability is confirmed. Finally, we have discussed the possible use of UV-Vis spectroscopy to (at least) confirm the change in the structure of the active site. Namely, UV-Vis spectroscopy has a long history in studying porphyrins, whose metallic centers have similar coordination as the SACs studied here. UV-Vis spectroscopy is fast and affordable and can be used *in operando* to monitor spectral changes associated with altered coordination of the metal center and its electronic structure.

Author Contributions: Conceptualization, Ana Dobrota and Igor Pašti; Formal analysis, Milica Ritopečki and Ana Dobrota; Funding acquisition, Natalia Skorodumova and Igor Pašti; Investigation, Milica Ritopečki and Ana Dobrota; Methodology, Ana Dobrota and Natalia Skorodumova; Resources, Natalia Skorodumova and Igor Pašti; Supervision, Igor Pašti; Validation, Natalia Skorodumova and Igor Pašti; Visualization, Ana Dobrota; Writing – original draft, Milica Ritopečki and Ana Dobrota; Writing – review & editing, Natalia Skorodumova and Igor Pašti.

Funding: This research was funded by the NATO Science for Peace and Security Programme (project OFICeR, G5729) and the Ministry of Education, Science, and Technological Development of the Republic of Serbia (Contract No. 451-03-9/2022-14/200146). I.A.P. is indebted to the Research Fund of the Serbian Academy of Sciences and Arts, project F-190, for supporting this study. The computations and data handling were enabled by resources provided by the Swedish National Infrastructure for Computing (SNIC) at the National Supercomputer Centre (NSC) at Linköping University, partially funded by the Swedish Research Council through grant agreement No. 2018-05973.

Data Availability Statement: Data are available upon reasonable request.

Conflicts of Interest: The authors declare no conflict of interest.

Appendix A

Table 2. The lowest pH on which H, O and OH can be found adsorbed on M@X_xN_yG. Dash marks that the given specie can not be found on M (as the most stable phase) for any pH value.

System	pH_{min} (H−M@X_xN_yG)	pH_{min} (OH−M@X_xN_yG)	pH_{min}(O−M@X_xN_yG)
Co@ON_3G	0.00	-	-
Co@O_2N_2G	6.03	-	-
Co@O_3NG	-	-	-
Co@SN_3G	0.00	-	-
Co@S_2N_2G	11.39	-	-
Co@S_3NG	4.64	-	-
Fe@ON_3G	0.00	7.29	13.61
Fe@O_2N_2G	13.51	-	-
Fe@O_3NG	-	-	-
Fe@SN_3G	0.00	7.81	-
Fe@S_2N_2G	9.58	-	-
Fe@S_3NG	13.85	-	-
Mn@ON_3G	2.76	10.59	-
Mn@O_2N_2G	-	7.71	-
Mn@O_3NG	-	10.81	-
Mn@SN_3G	2.23	12.56	-
Mn@S_2N_2G	-	-	-
Mn@S_3NG	-	-	-

References

1. Wu, X.; Zhang, H.; Zuo, S.; Dong, J.; Li, Y.; Zhang, J.; Han, Y. Engineering the Coordination Sphere of Isolated Active Sites to Explore the Intrinsic Activity in Single-Atom Catalysts. *Nano-Micro Lett.* **2021**, *13*, https://doi.org/10.1007/s40820-021-00668-6.
2. Cha, G.; Hwang, I.; Hejazi, S.; Dobrota, A.S.; Pašti, I.A.; Osuagwu, B.; Kim, H.; Will, J.; Yokosawa, T.; Badura, Z.; et al. As a Single Atom Pd Outperforms Pt as the Most Active Co-Catalyst for Photocatalytic H2 Evolution. *iScience* **2021**, *24*, 102938, doi:10.1016/j.isci.2021.102938.
3. Zhang, H.; Lu, X.F.; Wu, Z.P.; Lou, X.W.D. Emerging Multifunctional Single-Atom Catalysts/Nanozymes. *ACS Cent. Sci.* **2020**, *6*, 1288-1301, doi:10.1021/acscentsci.0c00512.
4. Liu, P.; Zhao, Y.; Qin, R.; Mo, S.; Chen, G.; Gu, L.; Chevrier, D.M.; Zhang, P.; Guo, Q.; Zang, D.; et al. Catalysis: Photochemical Route for Synthesizing Atomically Dispersed Palladium Catalysts. *Science* **2016**, *352*, 797-800, doi:10.1126/science.aaf5251.
5. Stamenkovic, V.R.; Fowler, B.; Mun, B.S.; Wang, G.; Ross, P.N.; Lucas, C.A.; Markovic, N.M. Improved Oxygen Reduction Activity on Pt3Ni(111) via Increased Surface Site Availability. *Science* **2007**, *315*, 493-497, doi:10.1126/science.1135941.
6. Stamenkovic, V.R.; Mun, B.S.; Arenz, M.; Mayrhofer, K.J.J.; Lucas, C.A.; Wang, G.; Ross, P.N.; Markovic, N.M. Trends in Electrocatalysis on Extended and Nanoscale Pt-Bimetallic Alloy Surfaces. *Nat. Mater.* **2007**, *6*, 241-247, doi:10.1038/nmat1840.
7. Stamenkovic, V.; Mun, B.S.; Mayrhofer, K.J.J.; Ross, P.N.; Markovic, N.M.; Rossmeisl, J.; Greeley, J.; Nørskov, J.K. Changing the Activity of Electrocatalysts for Oxygen Reduction by Tuning the Surface Electronic Structure. *Angew. Chemie* **2006**, *118*, 2897-2901, doi:10.1002/ange.200504386.
8. Holst-Olesen, K.; Silvioli, L.; Rossmeisl, J.; Arenz, M. Enhanced Oxygen Reduction Reaction on Fe/N/C Catalyst in Acetate Buffer Electrolyte. *ACS Catal.* **2019**, *9*, 3082-3089, doi:10.1021/acscatal.8b04609.
9. Holby, E.F.; Taylor, C.D. Activity of N-Coordinated Multi-Metal-Atom Active Site Structures for Pt-Free Oxygen Reduction Reaction Catalysis: Role of ∗OH Ligands. *Sci. Rep.* **2015**, *5*, 9286, doi:10.1038/srep09286.
10. Svane, K.L.; Reda, M.; Vegge, T.; Hansen, H.A. Improving the Activity of M−N4 Catalysts for the Oxygen Reduction Reaction by Electrolyte Adsorption. *ChemSusChem* **2019**, *12*, 5133-5141, doi:10.1002/cssc.201902443.
11. Jia, Q.; Ramaswamy, N.; Hafiz, H.; Tylus, U.; Strickland, K.; Wu, G.; Barbiellini, B.; Bansil, A.; Holby, E.F.; Zelenay, P.; et al. Experimental Observation of Redox-Induced Fe-N Switching Behavior as a Determinant Role for Oxygen Reduction Activity. *ACS Nano* **2015**, *9*, 12496-12505, doi:10.1021/acsnano.5b05984.
12. Nematollahi, P.; Barbiellini, B.; Bansil, A.; Lamoen, D.; Qingying, J.; Mukerjee, S.; Neyts, E.C. Identification of a Robust and Durable FeN4Cx Catalyst for ORR in PEM Fuel Cells and the Role of the Fifth Ligand. *ACS Catal.* **2022**, *12*, 7541–7549, doi:10.1021/acscatal.2c01294.
13. Zhong, W.; Wang, Z.; Han, S.; Deng, L.; Yu, J.; Lin, Y.; Long, X.; Gu, M.; Yang, S. Identifying the Active Sites of a Single Atom Catalyst with PH-Universal Oxygen Reduction Reaction Activity. *Cell Reports Phys. Sci.* **2020**, *1*, 100115, doi:10.1016/j.xcrp.2020.100115.
14. Li, Y.; Wu, Z.S.; Lu, P.; Wang, X.; Liu, W.; Liu, Z.; Ma, J.; Ren, W.; Jiang, Z.; Bao, X. High-Valence Nickel Single-Atom Catalysts Coordinated to Oxygen Sites for Extraordinarily Activating Oxygen Evolution Reaction. *Adv. Sci.* **2020**, *7*, 1903089, doi:10.1002/advs.201903089.
15. Song, P.; Luo, M.; Liu, X.; Xing, W.; Xu, W.; Jiang, Z.; Gu, L. Zn Single Atom Catalyst for Highly Efficient Oxygen Reduction Reaction. *Adv. Funct. Mater.* **2017**, *27*, 1700802, doi:10.1002/adfm.201700802.
16. Zhang, Z.; Feng, C.; Li, X.; Liu, C.; Wang, D.; Si, R.; Yang, J.; Zhou, S.; Zeng, J. In-Situ Generated High-Valent Iron Single-Atom Catalyst for Efficient Oxygen Evolution. *Nano Lett.* **2021**, *21*, 4791-4801, doi:10.1021/acs.nanolett.1c01335.
17. Zitolo, A.; Goellner, V.; Armel, V.; Sougrati, M.T.; Mineva, T.; Stievano, L.; Fonda, E.; Jaouen, F. Identification of Catalytic Sites for Oxygen Reduction in Iron- and Nitrogen-Doped Graphene Materials. *Nat. Mater.* **2015**, *14*, 937-942, doi:10.1038/nmat4367.
18. Jung, E.; Shin, H.; Lee, B.H.; Efremov, V.; Lee, S.; Lee, H.S.; Kim, J.; Hooch Antink, W.; Park, S.; Lee, K.S.; et al. Atomic-Level Tuning of Co–N–C Catalyst for High-Performance Electrochemical H2O2 Production. *Nat. Mater.* **2020**, *19*, 436-442, doi:10.1038/s41563-019-0571-5.
19. Yang, G.; Zhu, J.; Yuan, P.; Hu, Y.; Qu, G.; Lu, B.A.; Xue, X.; Yin, H.; Cheng, W.; Cheng, J.; et al. Regulating Fe-Spin State by Atomically Dispersed Mn-N in Fe-N-C Catalysts with High Oxygen Reduction Activity. *Nat. Commun.* **2021**, *12*, 1734, doi:10.1038/s41467-021-21919-5.
20. Choi, C.H.; Choi, W.S.; Kasian, O.; Mechler, A.K.; Sougrati, M.T.; Brüller, S.; Strickland, K.; Jia, Q.; Mukerjee, S.; Mayrhofer, K.J.J.; et al. Unraveling the Nature of Sites Active toward Hydrogen Peroxide Reduction in Fe-N-C Catalysts. *Angew. Chemie - Int. Ed.* **2017**, *56*, 8809-8812, doi:10.1002/anie.201704356.
21. Marković, N.M.; Ross, P.N. Surface Science Studies of Model Fuel Cell Electrocatalysts. *Surf. Sci. Rep.* **2002**, *45*, 117-229, doi:10.1016/s0167-5729(01)00022-x.
22. Dobrota, A.S.; Đokić, T.; Skorodumova, N. V.; Mentus, S. V.; Pašti, I.A. What Is the Real State of Single-Atom Catalysts under Electrochemical Conditions—From Adsorption to Surface Pourbaix Plots? *Catalysts* **2021**, *11*, 1207, doi:10.3390/catal11101207.
23. Dobrota, A.S.; Skorodumova, N. V.; Mentus, S. V.; Pašti, I.A. Surface Pourbaix Plots of M@N4-Graphene Single-Atom Electrocatalysts from Density Functional Theory Thermodynamic Modelling. *Electrochim. Acta* **2022**, *412*, doi.org/10.48550/arXiv.2111.14269.

24. Zeng, Z.; Chan, M.K.Y.; Zhao, Z.J.; Kubal, J.; Fan, D.; Greeley, J. Towards First Principles-Based Prediction of Highly Accurate Electrochemical Pourbaix Diagrams. *J. Phys. Chem. C* **2015**, *119*, 18177-18187, doi:10.1021/acs.jpcc.5b03169.
25. Marenich, A. V.; Majumdar, A.; Lenz, M.; Cramer, C.J.; Truhlar, D.G. Construction of Pourbaix Diagrams for Ruthenium-Based Water-Oxidation Catalysts by Density Functional Theory. *Angew. Chemie - Int. Ed.* **2012**, *51*, 12810-12814, doi:10.1002/anie.201206012.
26. Hansen, H.A.; Rossmeisl, J.; Nørskov, J.K. Surface Pourbaix Diagrams and Oxygen Reduction Activity of Pt, Ag and Ni(111) Surfaces Studied by DFT. *Phys. Chem. Chem. Phys.* **2008**, *10*, 3722-3730, doi:10.1039/b803956a.
27. Kresse, G.; Furthmüller, J. Efficient Iterative Schemes for Ab Initio Total-Energy Calculations Using a Plane-Wave Basis Set. Phys. Rev. B - Condens. Matter Mater. Phys. **1996**, *54*, 11169-11186, doi:10.1103/PhysRevB.54.11169.
28. Kresse, G.; Furthmüller, J. Efficiency of Ab-Initio Total Energy Calculations for Metals and Semiconductors Using a Plane-Wave Basis Set. *Comput. Mater. Sci.* 1996, *6*, doi:10.1016/0927-0256(96)00008-0.
29. Kresse, G.; Hafner, J. Ab Initio Molecular Dynamics for Liquid Metals. *Phys. Rev. B* **1993**, *47*, 558-561, doi:10.1103/PhysRevB.47.558.
30. Blöchl, P.E. Projector Augmented-Wave Method. *Phys. Rev. B* **1994**, *50*, 17953-17979, doi:10.1103/PhysRevB.50.17953.
31. Grimme, S.; Antony, J.; Ehrlich, S.; Krieg, H. A Consistent and Accurate Ab Initio Parametrization of Density Functional Dispersion Correction (DFT-D) for the 94 Elements H-Pu. *J. Chem. Phys.* **2010**, *132*, 154104, doi:10.1063/1.3382344.
32. Monkhorst, H.J.; Pack, J.D. Special Points for Brillouin-Zone Integrations. Phys. Rev. B 1976, *13*, doi:10.1103/PhysRevB.13.5188.
33. Momma, K.; Izumi, F. VESTA: A Three-Dimensional Visualization System for Electronic and Structural Analysis. *J. Appl. Crystallogr.* **2008**, *41*, 653-658, doi:10.1107/S0021889808012016.
34. Nørskov, J.K.; Rossmeisl, J.; Logadottir, A.; Lindqvist, L.; Kitchin, J.R.; Bligaard, T.; Jónsson, H. Origin of the Overpotential for Oxygen Reduction at a Fuel-Cell Cathode. *J. Phys. Chem. B* **2004**, *108*, 17886-17892, doi:10.1021/jp047349j.
35. Gajdoš, M.; Hummer, K.; Kresse, G.; Furthmüller, J.; Bechstedt, F. Linear Optical Properties in the Projector-Augmented Wave Methodology. *Phys. Rev. B - Condens. Matter Mater. Phys.* **2006**, 73, 045112, doi:10.1103/PhysRevB.73.045112.
36. Kittel, C. Crystal Binding and Elastic Constants. In Introduction to Solid State Physics, 8th Edition; Johnson, S., Eds.; Publisher: Wiley & Sons New Jersey, USA, 2004; pp. 50.
37. Nørskov, J.K.; Bligaard, T.; Logadottir, A.; Kitchin, J.R.; Chen, J.G.; Pandelov, S.; Stimming, U. Trends in the Exchange Current for Hydrogen Evolution. *J. Electrochem. Soc*. **2005**, *152*, J23, doi:10.1149/1.1856988.
38. M Ganose, A.; J Jackson, A.; O Scanlon, D. Sumo: Command-Line Tools for Plotting and Analysis of Periodic Ab Initio Calculations. *J. Open Source Softw*. **2018**, *3*, 717, doi:10.21105/joss.00717.
39. Sun, Z.C.; She, Y. Bin; Zhou, Y.; Song, X.F.; Li, K. Synthesis, Characterization and Spectral Properties of Substituted Tetraphenylporphyrin Iron Chloride Complexes. *Molecules* **2011**, *16*, 2960-2970, doi:10.3390/molecules16042960.
40. Rayati, S.; Ruzbahani, S.E.; Nejabat, F. A Comparative Study of Catalytic Activity of Fe, Mn and Cu Porphyrins Immobilized on Mesoporous MCM-41 in Oxidation of Sulfides. *Macroheterocycles* **2017**, *10*, 62-67, doi:10.6060/mhc170186r.
41. Giovannetti, R. The Use of Spectrophotometry UV-Vis for the Study of Porphyrins. In Macro To Nano Spectroscopy; Uddin, J., Eds.; Publisher: IntechOpen London, United Kingdom, 2012; pp. 87-108.